PERGAMON

Carbon 39 (2001) 1543–1555

CARBON

# Preparation of activated carbon fibres from acrylic textile fibres

P.J.M. Carrott[a,*], J.M.V. Nabais[a], M.M.L. Ribeiro Carrott[a], J.A. Pajares[b]

[a]*Departamento de Química, Universidade de Évora, Colégio Luís António Verney, 7000-671 Évora, Portugal*
[b]*Instituto Nacional del Carbón, CSIC, Apartado 73, 33080 Oviedo, Spain*

Received 5 August 2000; accepted 30 September 2000

**Abstract**

Acrylic textile fibres have been used to prepare activated carbon fibres (ACF). Characterisation by means of elemental analysis, XRD, SEM and low temperature nitrogen adsorption show that the properties of the acrylic ACF compare favourably with those of non-textile PAN, Kevlar and Nomex ACF. A particularly interesting, and never previously reported, feature was observed with fibres activated at 900°C. It was found, with one fibre in particular, that over a very limited range of burn-off between 40 and 50% the micropore volume tripled, the mean pore width suddenly increased, the mean stack height, $L_c$, suddenly decreased and the reactivity decreased by more than a half. The observed changes suggest a change in the mechanism of activation from one involving principally gasification of amorphous or more reactive carbon at low burn-off to one involving principally attack of individual crystallites and their reorganisation at higher burn-off. 

*Keywords:* A. Activated carbon; Carbon fibers; Molecular sieves; C. Adsorption; X-ray diffraction

## 1. Introduction

Activated carbon fibres (ACF) are a comparatively modern form of porous carbon material with a number of significant advantages over the more traditional powder or granular forms. These include high surface area and adsorption capacity, as well as very high rates of adsorption from the gas or liquid phase [1–3]. The micropore size is in general uniform and can often be controlled by adjusting the conditions of preparation of the fibres or by post-preparation modification. Furthermore, by appropriate pre-activation impregnation with, for example, phosphates, boric acid or certain transition metal oxo-complexes [4–8], or by inclusion of carbon black in the polymer mix [9], it is also possible to introduce different types of mesoporosity. Their versatility is further enhanced by the possibility of confining the fibres in various physical forms. For example, ACFs are currently available commercially in the form of fibre tows, fabrics and felts. Hollow fibres have been produced in the laboratory [10,11] and new physical presentations, namely porous activated carbon fibre composite monoliths, have also been more recently developed [12,13]. These physical characteristics and adsorption properties of ACF have permitted the development of a number of new carbon material applications such as antibacterial wound dressings [14–16], disposable gas masks, methane storage [17] and polarizable electrodes [18], as well as the use of ACF in more traditional adsorption separation and catalysis applications, such as solvent recovery, $SO_x$ and $NO_x$ removal [3,19,20], and gas separation [10,11]. In all cases, the ACF can in principle simultaneously provide higher efficiencies with simplified process equipment design [21].

Some of the precursors which have been used for the preparation of ACF include fibres spun from phenolic resins [2,16,18,20,22–24], polyimides [11], polyarylamides [21,25–29] and pitch [2,3,12,15,19,24,30–34], as well as from cellulose based fibres [2–8,30,31,35–39] and polyacrylonitrile based fibres [2,3,9,12,13,40–50]. The latter are of particular interest due to the fact that acrylic fibres are currently the principal precursor used in the production of high performance engineering carbon fibres [51]. Hence, a considerable amount of work has already been published on the microstructure of the fibres as well as on the structural and chemical transformations occurring at all stages of production from the initial polyacrylonitrile copolymer right up to the final carbon fibre [51]. A second point of particular interest, and that which originated the

*Corresponding author. Tel.: +351-266-745-311; fax: +351-266-744-971.

*E-mail address:* peter@uevora.pt (P.J.M. Carrott).

0008-6223/01/$ – see front matter 
PII: S0008-6223(00)00271-2

current work, is the fact that acrylic fibres are also one of the principal textile fibres. There are obviously differences between the precursors used for high performance carbon fibre manufacture and textile fibres in relation to, for example, the comonomer used and the fibre cross-section. It is known, however, that other textile fibres, in particular viscose rayon fibres, make excellent ACFs and the available evidence suggests that textile grade acrylic fibres also make good precursors.

We will present here results of the structural characterisation of ACFs obtained from textile fibres which consisted principally of acrylonitrile and vinyl acetate. The vinyl acetate is introduced in order to simplify the fibre processing and to improve the properties of the textile fibre. However, the presence of comonomer is also very important during the preparation of ACFs, as it leads to a reduction in the initial temperature of dehydrogenation and of cyclisation of the nitrile groups and hence accelerates the thermal stabilisation of the polymer backbone [44]. This ultimately also improves the physical properties of the carbonised fibre. In contrast, in the absence of comonomer the cyclisation is much slower and the fibres produced have much poorer mechanical properties [45].

The precise effect of the comonomer is sensitive to its exact nature and the quantity present. For instance, it has been shown that the rate of thermal decomposition varies in the order PAN<PAN/vinyl acetate<PAN/acrylamide~PAN/methacrylic acid [47–50]. We would also expect that the exact conditions used for the stabilisation of the fibres would have some influence on the properties of the ACF. In addition, as the properties of the acrylic fibre are sensitive to the exact process conditions, such as the degree of stretching during spinning [50], we would also expect that the properties of the ACF would be sensitive to these factors too. We will show that although the chemical composition of our fibre samples is very similar, the underlying microstructure is subtly different and consequently the development of the microporosity as a function of burn-off shows some interesting variations, which are also mirrored by the variation in a number of other parameters.

## 2. Materials

The precursors used for the production of ACF were three acrylic textile fibres provided by Fisipe (Barreiro, Portugal). According to the manufacturer all of the fibres had been polymerised from acrylonitrile (~90 w%) and vinyl acetate (~10 w%) monomers. Fibres F1 and F1N were bright 3 denier (3 m/mg) filaments of varying length produced in 1995 (F1) and 1999 (F1N) with slightly different fabrication processes. Fibre F2 was also produced in 1995 but was in the form of matte 3 denier filaments of ~60 mm length. This latter fibre also contained trace quantities of a titanium dioxide optical brightener.

For the production of the ACF a horizontal tubular furnace made by Termolab and with Eurotherm 904 temperature controllers and a 1 m tubular ceramic insert was used. The internal temperature of the furnace was first calibrated and the length and position of the constant temperature hot zone determined. About 12 g of fibre were placed in a 10 cm stainless steel boat with perforated ends to facilitate gas flow and this positioned in the centre of the constant temperature zone. Stabilisation of the fibres was carried out by heating to 300°C at a rate of 1°C $min^{-1}$ under a constant $N_2$ flow of 85 $cm^3$ $min^{-1}$ and maintaining for 2 h. The fibres were then carbonised by raising the temperature at a rate of 5°C $min^{-1}$ to 800°C and maintaining at that temperature for 1 h. The carbonisation yield, in relation to the initial mass of unstabilised fibre, was 50–52 w%. Activation was carried out by raising the temperature again by 15°C $min^{-1}$ to 900°C and then switching to a $CO_2$ flow of 85 $cm^3$ $min^{-1}$, maintaining for the appropriate time in order to obtain burn-offs within the range 10–90 w% (indicated in the sample designations), switching back to the $N_2$ flow and allowing to cool to below 50°C before removing the ACF from the furnace and storing in a sealed sample flask. A series of ACF was also obtained from fibre F1 by activation at 800°C. The conditions used and the corresponding sample designations are indicated in Table 1.

## 3. Experimental

Nitrogen adsorption isotherms at 77 K were determined using a CE Instruments Sorptomatic 1990 after outgassing the samples at 380°C for 2 h to a residual vacuum of $5\times10^{-6}$ mbar.

Elemental analysis of carbon, hydrogen, sulphur, nitrogen and oxygen was carried out using a Eurovector EuroEA elemental analyser. No evidence for the presence of sulphur was found. The quantities of the other elements are included in Table 1.

X-ray powder diffraction patterns were determined at INCAR (Oviedo, Spain) using a Siemens D5000 diffractometer with Cu Kα radiation ($\lambda=0.15406$ nm) at a step size of 0.01°.

Scanning electron micrographs carried out in secondary electron imaging mode were also measured at INCAR (Oviedo, Spain), after plating the samples with gold, using a Zeiss DSM-942.

## 4. Results

### *4.1. Elemental analysis*

If we assume that all of the nitrogen present in the original fibres comes from the acrylonitrile (AN) monomer and that all of the oxygen comes from the vinyl acetate

Table 1
Conditions of activation and elemental analysis of ACF samples[a]

| Sample | Activation time h | Burn-off w% | N w% | C w% | H w% | O w% |
|---|---|---|---|---|---|---|
| Fibre F1 at 900°C | | | | | | |
| F1 | o.f. | – | 26.323 | 64.213 | 5.910 | 3.546 |
| F1-0 | 0 | 0 | 16.466 | 74.936 | 1.013 | 9.634 |
| F1-14 | 0.5 | 14 | 9.676 | 78.376 | 0.773 | 10.537 |
| F1-23 | 1 | 23 | 8.930 | 77.141 | 0.967 | 11.901 |
| F1-37 | 2 | 37 | 8.440 | 80.954 | 0.600 | 11.544 |
| F1-40 | 3 | 40 | 5.924 | 80.198 | 0.447 | 16.438 |
| F1-53 | 5 | 53 | 5.614 | 82.175 | 0.465 | 12.974 |
| F1-64 | 8 | 64 | 4.211 | 84.499 | 0.400 | 6.734 |
| F1-76 | 9 | 76 | 4.169 | 80.039 | 0.297 | 7.724 |
| F1-90 | 12 | 90 | 4.169 | 81.427 | 0.345 | 5.492 |
| Fibre F1 at 800°C | | | | | | |
| F1 | o.f. | – | 26.323 | 64.213 | 5.910 | 3.546 |
| F1-0 | 0 | 0 | 16.466 | 74.936 | 1.013 | 9.634 |
| F1-8-10 | 1 | 10 | 11.006 | 72.697 | 1.250 | 13.151 |
| F1-8-11 | 2 | 11 | 10.886 | 78.650 | 0.997 | 9.732 |
| F1-8-22 | 5 | 22 | 9.181 | 84.201 | 0.889 | 8.12 |
| F1-8-32 | 9 | 32 | 8.302 | 81.906 | 0.917 | 10.306 |
| F1-8-50 | 14 | 50 | 7.412 | 80.860 | 0.970 | 11.538 |
| F1-8-52 | 18 | 52 | 5.804 | 77.233 | 0.547 | 13.986 |
| F1-8-61 | 25 | 61 | 5.358 | 79.367 | 0.656 | 10.600 |
| F1-8-77 | 36 | 77 | 5.029 | 78.705 | 0.546 | 10.211 |
| Fibre F1N at 900°C | | | | | | |
| F1N | o.f. | – | 22.923 | 64.646 | 5.472 | 4.312 |
| F1N-0 | 0 | 0 | 12.617 | 79.254 | 0.967 | 7.445 |
| F1N-12 | 1 | 12 | 6.896 | 77.746 | 0.872 | 13.184 |
| F1N-25 | 1.5 | 25 | 5.615 | 83.189 | 0.399 | 11.049 |
| F1N-36 | 2 | 36 | 5.711 | 84.130 | 0.421 | 11.421 |
| F1N-40 | 3 | 40 | 4.692 | 85.936 | 0.416 | 12.610 |
| F1N-51 | 5 | 51 | 3.742 | 80.697 | 0.362 | 12.769 |
| F1N-61 | 7 | 61 | 4.836 | 83.130 | 0.509 | 8.701 |
| F1N-85 | 9 | 85 | 4.110 | 84.661 | 0.364 | 7.895 |
| Fibre F2 at 900°C | | | | | | |
| F2 | o.f. | – | 23.359 | 64.573 | 5.771 | 4.264 |
| F2-0 | 0 | 0 | 11.776 | 77.895 | 0.825 | 6.926 |
| F2-12 | 1 | 12 | 7.306 | 77.750 | 0.462 | 11.340 |
| F2-26 | 2 | 26 | 5.312 | 81.991 | 0.343 | 10.484 |
| F2-30 | 2.5 | 30 | 6.034 | 82.533 | 0.382 | 7.852 |
| F2-41 | 3 | 41 | 4.437 | 82.567 | 0.340 | 8.185 |
| F2-48 | 5 | 48 | 3.970 | 82.312 | 0.346 | 9.242 |
| F2-66 | 7 | 66 | 3.859 | 76.470 | 0.232 | 7.570 |
| F2-74 | 8 | 74 | 3.953 | 76.094 | 0.251 | 11.148 |
| F2-94 | 9 | 94 | 3.328 | 81.686 | 0.328 | 7.562 |

[a] (o.f. = original acrylic fibre).

(VA) monomer, then we can make an estimate of the fibre composition from the relationships:

$$AN = (53/14) \times \%N \times 100/\{(53/14) \times \%N + (86/32) \times \%O\} \quad (1)$$

$$VA = (86/32) \times \%O \times 100/\{(53/14) \times \%N + (86/32) \times \%O\} \quad (2)$$

where 53 and 86 are the molar masses of AN and VA, 14 and 32 are the masses of nitrogen and oxygen in one mole

of AN and VA, and %N and %O are the mass percentages of nitrogen and oxygen in the fibre as given in Table 1. The results obtained, which are approximate as the small quantities of other additives, such as titanium dioxide in the case of fibre F2, are not taken into consideration are the following: F1 contains 91.3% AN + 8.7% VA, F1N contains 88.2% AN + 11.8% VA, F2 contains 88.5% AN + 11.5% VA. Hence, the results indicate that the fibres F1N and F2 have virtually the same composition, whereas F1 contains a higher proportion of acrylonitrile monomer and rather less comonomer.

During the stabilisation and carbonisation of the fibres the nitrogen content is approximately halved and the hydrogen content decreases approximately fivefold, while there are correspondingly large increases in the carbon and, in particular, the oxygen contents. During activation the elemental composition continues to change. However, even at the highest burn-offs the fibres still contain significant amounts of nitrogen (~3–4%) and oxygen (~5–8%).

### 4.2. SEM

Two representative scanning electron micrographs are shown for a carbonised fibre in Fig. 1 and an activated fibre in Fig. 2. The original fibres have a kidney bean cross-section and it can be seen from Figs. 1 and 2 that this is preserved during carbonisation and activation. The cross sectional dimensions are about 25×15 μm in each case. The external surface of the ACFs was slightly corrugated and submicron sized pits, fairly uniformly distributed, were gradually formed during activation. It was not possible to carry out elemental analysis of the fibre surface. However, there was no direct evidence from SEM of any catalytic effect arising from the presence of titania particles or other metallic impurities. A more detailed SEM study will be presented in a separate paper.

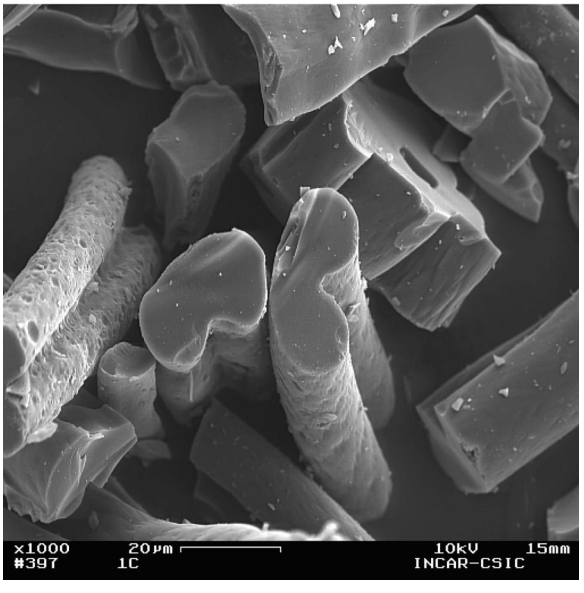


Fig. 1. SEM image of carbonised F1.

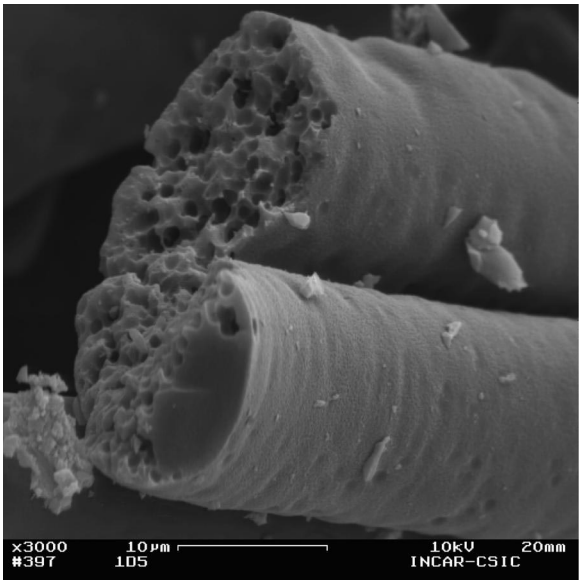


Fig. 2. SEM image of fibre F1, activated to 53%.

### 4.3. Reactivity

The variation of burn-off with time of activation is shown in Fig. 3. As would be expected, the rate of burn-off is much lower when the activation is carried out at 800°C than at 900°C. On the other hand, a surprising feature of

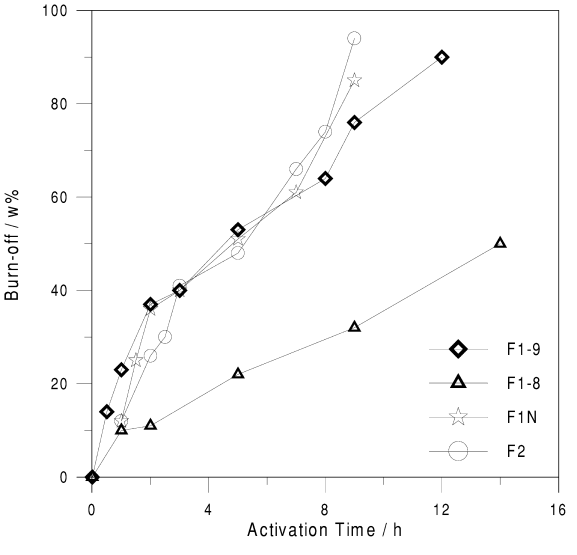


Fig. 3. Burn-off as a function of activation time.

the plots is that they appear to indicate the existence of two distinct regimes of reactivity. At the lower activation temperature, the first regime extends up to a burn-off of ~50%, and the second regime, which is not shown on Fig. 3, extends from 50% up to the highest burn-off achieved at this temperature. In each regime the plot is linear, and from the slopes we can calculate rates of activation of 3.7 and 1.2 mg $min^{-1}$. At the higher activation temperature of 900°C, the plots for the three different fibres are quite similar and also show the two regimes of reactivity. However, the first regime only extends up to about 35% burn-off, while the second regime extends from 35% upwards. At higher burn-offs, there is some indication that the plots for F1N and F2 begin to swing upwards again, which would indicate an increase in the rate of activation. However, over the two initial regimes the plots are linear and from the slopes we can calculate activation rates of 20.2, 17.1 and 13.5 mg $min^{-1}$ for the fibres F1, F1N and F2, respectively, decreasing to 5.5 mg $min^{-1}$ for all three fibres above 40% burn-off.

### 4.4. XRD

Representative XRD patterns of the samples are given in Fig. 4. In all cases the two peaks due to reflections from the (*002*) and (*10*) planes are clearly visible. In addition, the XRD pattern of F2 contains peaks due to the titania additive which, by their sharpness, indicate that the titania is present as comparatively large, although still sub-micron, particles.

From the position of the (*002*) peak we can calculate an estimate of the interplanar spacing, $d_{002}$, by direct application of Bragg's Law. The values are given in Table 2 for F1 and F1N and are ~0.360±0.003 nm being practically unchanged over the range of burn-off from 0 up to 60–70%. It was not possible to obtain estimates of the $d_{002}$ spacings for F2, due to overlap of the titania peaks. However, it is probably reasonable to assume that they do not differ significantly from the values given by F1 and F1N.

Estimates of mean crystallite dimensions can generally be obtained from powder XRD data by application of the

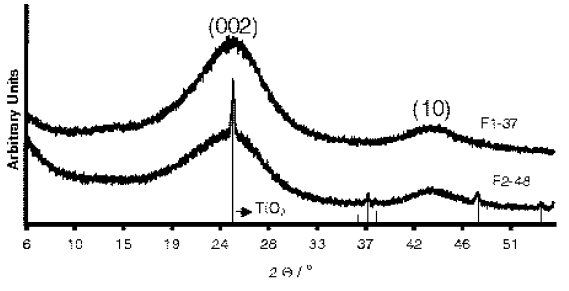


Fig. 4. Representative XRD patterns for samples F1-37 and F2-48.

Table 2
Results of characterisation by XRD measurements[a]

| Sample | $d_{002}$ nm | $L_a$ nm | $L_c$ nm | $N_p$ |
|---|---|---|---|---|
| F1-0 | 0.357 | 4.699 | 1.254 | 3.5 |
| F1-37 | 0.356 | 4.135 | 1.256 | 3.5 |
| F1-53 | 0.361 | 4.528 | 1.182 | 3.2 |
| F1-76 | 0.363 | 5.129 | 1.195 | 3.2 |
| F1N-0 | 0.357 | 3.831 | 1.321 | 3.7 |
| F1N-12 | 0.357 | 4.199 | 1.305 | 3.6 |
| F1N-36 | 0.363 | 4.218 | 1.189 | 3.3 |
| F1N-61 | 0.364 | 4.670 | 1.170 | 3.2 |
| F2-0 | n.d. | 5.702 | 1.312 | 3.6 |
| F2-26 | n.d. | 6.385 | 1.313 | 3.6 |
| F2-48 | n.d. | 6.113 | 1.163 | 3.2 |
| F2-77 | n.d. | 6.936 | 1.131 | 3.1 |

[a] n.d. = not determined. $N_p$ = mean number of layer planes.

Debye–Scherrer Equation. When applied to carbon materials, the equation takes the forms [52]:

$$L_c = 0.90\lambda/\beta \cos \theta_{002} \quad (3)$$

$$L_a = 1.94\lambda/\beta \cos \theta_{10} \quad (4)$$

with $\beta$ equal to the peak width at half height corrected for instrumental broadening. $L_c$ and $L_a$ are not exactly equal to the height and width of the crystallites, but can be used as convenient relative estimates of these quantities [53]. The true crystallite size is likely to be slightly greater than the calculated values.

The calculated values are given in Table 2. It should also be noted from Table 2 that in all cases the change in $L_c$ is not continuous. For each sample, the two values at low burn-off are similar and the two values at higher burn off are similar to each other but significantly lower than the low burn-off values.

Further consideration of the results in Table 2 indicates that, apart from the similar type of behaviour already referred to, there are some small quantitative differences between the fibres. Comparing similar levels of burn-off, F2 tends to give slightly lower $L_c$ than F1N. F1 gives even lower values at lower degrees of burn-off. However, the variation in $L_c$ is less pronounced for this sample and, at the higher levels of burn-off, F1 gives similar values to F1N, both being a little higher than the $L_c$ values given by F2.

With regard to the crystallite width, $L_a$ is significantly greater for F2 than for the other fibres at all levels of burn-off. F1N has the lowest $L_a$ value of the carbonised samples, but the activated F1 and F1N give almost identical values. In general terms, the results indicate that $L_a$ increases monotonically with increase in burn-off.

At first sight the decrease in $L_c$ would appear to be inconsistent with the constant $d_{002}$ spacing. The only reasonable explanation for the observed change appears to

be a decrease in the mean number of layer planes in the crystallites and we can obtain a relative estimate of this number for each sample from the ratio $N_p = L_c/d_{002}$. The values obtained, using the constant value $d_{002} = 0.360$ nm for F2, are included in Table 2. As already mentioned, the $L_c$ values are lower than the true crystallite heights, and the $N_p$ values will therefore also be somewhat lower than the true mean number of layer planes in the crystallites. It is evident, however, that with increase in the degree of burn-off from (approximately) <40% to >40% the mean number of layer planes in the crystallites decreases by ~10–15%.

### 4.5. $N_2$ adsorption at 77 K

The nitrogen adsorption isotherms determined on the three fibres are shown in Figs. 5–8. It can be seen that the isotherms are all Type I with very low slope in the multilayer region indicating a low external surface area. The isotherms were also reversible except for that determined on F2-12, where a molecular sieving effect was observed. As the degree of burn-off increased, the level of uptake also increased. However, for F1 activated at 800 or 900°C, there was a decreased level of uptake at the highest burn-offs. This decrease at high burn-off is not very common behaviour, although it has previously been reported for Kevlar ACF [25]. In all cases the knee of the isotherm becomes more rounded as the burn-off increases, indicating an increase in the mean pore width which does not appear, however, to extend beyond the micropore range for any of the fibres at any burn-off.

The isotherms were analysed by means of the $\alpha_s$ method using previously published standard data for the adsorption of $N_2$ on carbon materials at 77 K [54], and a representative series of plots for F1 are given in Fig. 9. In all cases, the $\alpha_s$ plots were found to give good linearity in the multilayer range and, from the slope and intercept, the values of external surface area and total micropore volume, given in Table 3, were calculated. DR plots were also constructed and a representative series of plots for F1 are given in Fig. 10. In general, it was found that the linearity of the plots was most extensive for the lower burn-off samples, while for the higher burn-off samples the plots

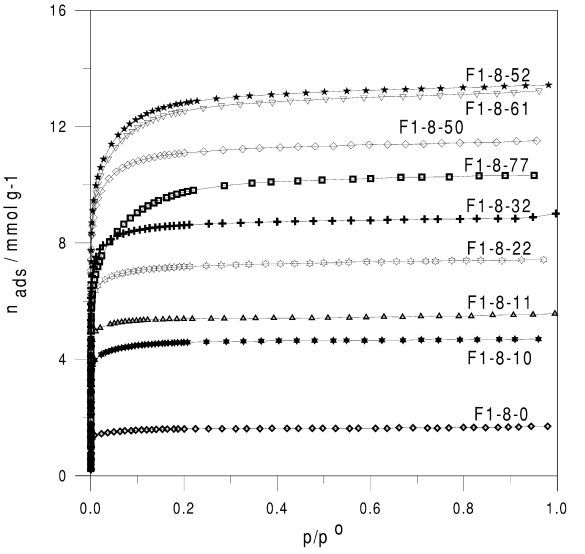


Fig. 6. Low temperature nitrogen adsorption/desorption isotherms determined on F1-8.

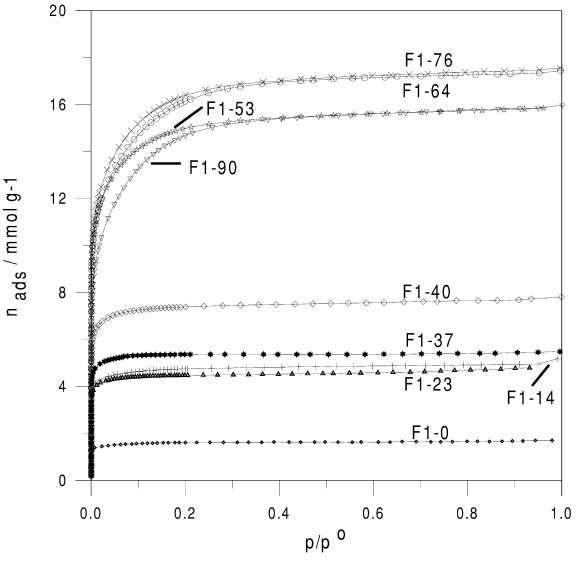


Fig. 5. Low temperature nitrogen adsorption/desorption isotherms determined on F1.

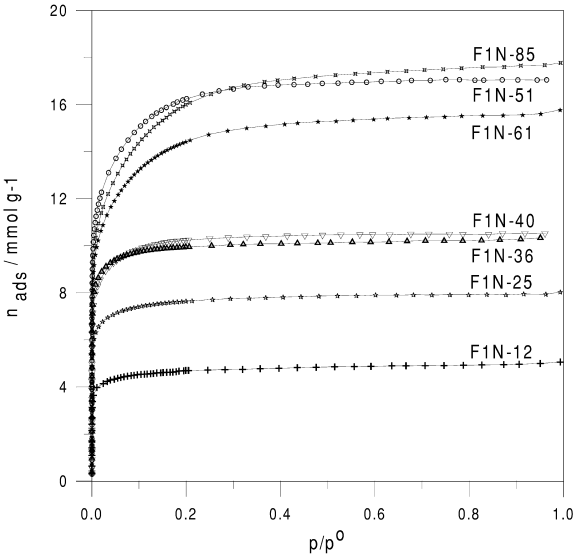


Fig. 7. Low temperature nitrogen adsorption/desorption isotherms determined on F1N.

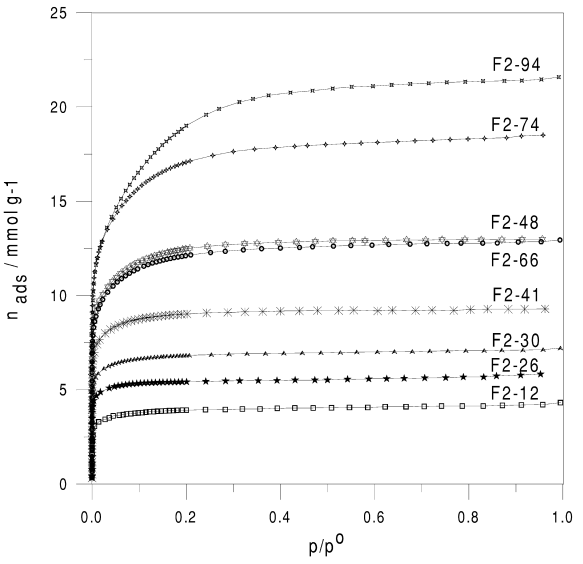


Fig. 8. Low temperature nitrogen adsorption/desorption isotherms determined on F2.

deviated from linearity at both low pressures and high pressures, indicating the simultaneous occurrence of pore widening and pore narrowing, as previously found with viscose rayon based charcoal cloths [39]. The values of micropore volume and characteristic energy calculated from the intercept and slope of each DR plot are given in Table 3. Also given are the estimates of mean pore width calculated from the relationship [55]:

$$L_o = 10.8/(E_o - 11.4) \quad (5)$$

The results in Table 3 confirm that the external surface area is low, and indicate a value of around $5\pm5\ m^2g^{-1}$ for all samples. The results in Table 3 also confirm that the pore volume generally increases with burn-off, with the exception of the higher burn-off samples of F1, where the pore volumes decrease, and those of F1N, where the pore volume remains constant. The values of $V_s$ and $V_o$ are in reasonable agreement at low burn-offs, but at burn-offs of $>40$–$50\%$ $V_s$ becomes significantly greater than $V_o$, indicating a widening of the pores into the region of secondary micropores. This is confirmed by the corresponding variation in the values of $L_o$, which, in most cases, vary from about 0.7–0.8 nm at low burn-off to about 1.2 nm at high burn-off.

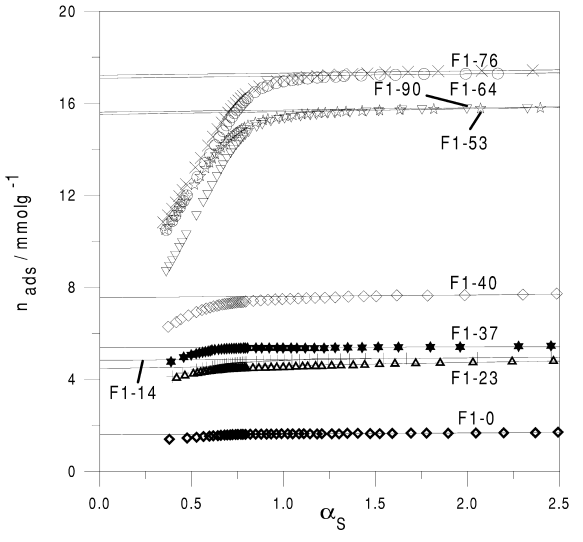


Fig. 9. Representative $\alpha_s$ plots for F1.

## 5. Discussion

### 5.1. Crystallite structure

The $d_{002}$ spacing of our samples is approximately 0.36 nm, which is within the range 0.35–0.37 nm generally found for ACFs [25,26,30,31,33,35,37,41]. All published $d_{002}$ values are greater than the value of 0.335 nm found in graphite due to the turbostratic nature of the crystallites and their thinness. The latter in particular leads to an overall reduction in the total carbon–carbon interaction energy. Carbon atoms in one layer interact with carbon atoms in adjacent layers by means of dispersion interactions which fall off rapidly with distance, but which only become insignificant when there are a large number of layers and when the ratio of basal face to internal planes is low. In ACFs the thickness of the crystallites is typically about 3–8 layers, which is evidently insufficient to maintain the graphite $d_{002}$ spacing. When the thickness of the crystallites is increased to more than about 5 nm, on the other hand, values closer to that of graphite have been obtained [35,41]. Lower values have also been reported for pitch ACF, which might be expected to have a more ordered crystallite structure than linear polymer derived ACFs [32,33].

The thickness of the crystallites of our samples, as estimated by the $L_c$ values, is comparable to results previously obtained with ACFs from PAN, Nomex and viscose rayon [26,37,41]. Pitch and phenolic resins tend to give slightly lower values [24,30–33], while Kevlar has been reported to give values about twice as high [25]. In the case of Kevlar and Nomex, $L_c$ has been found to decrease on passing from the carbonised char to low burn-off activated samples, but then to increase with increasing burn-off [25,26]. In contrast, we find with our samples that $L_c$ always decreases with increasing burn-off, there being a particularly significant transition at about 40% burn-off for the 900° activated samples. Other authors have found that the exact value of $L_c$ also depends on other factors, such as the exact preparative conditions and post-preparation thermal treatments. For example, Kumar et al.

Table 3
Textural characteristics of the original fibres and activated carbon fibres[a]

| Sample | $S_{BET}$ $m^2g^{-1}$ | $\alpha_s$ Method | | DR Method | | |
|---|---|---|---|---|---|---|
| | | $V_s$ $cm^3g^{-1}$ | $S_{ext}$ $m^2g^{-1}$ | $V_o$ $cm^3g^{-1}$ | $E_o$ kJ $mol^{-1}$ | $L_o$ nm |
| F1-0 | 130.5 | 0.06 | 1.55 | 0.05 | 25.97 | 0.741 |
| F1-14 | 393.7 | 0.17 | 3.29 | 0.16 | 24.81 | 0.806 |
| F1-23 | 330.2 | 0.16 | 8.50 | 0.16 | 26.02 | 0.739 |
| F1-37 | 390.0 | 0.18 | 6.12 | 0.19 | 26.1 | 0.735 |
| F1-40 | 613.5 | 0.26 | 4.77 | 0.25 | 25.84 | 0.748 |
| F1-53 | 1238.6 | 0.54 | 7.95 | 0.46 | 20.76 | 1.154 |
| F1-64 | 1313.6 | 0.59 | 6.03 | 0.46 | 19.81 | 1.284 |
| F1-76 | 1341.3 | 0.60 | 6.02 | 0.49 | 19.85 | 1.278 |
| F1-90 | 1213.4 | 0.54 | 5.89 | 0.43 | 16.58 | 2.085 |
| F1-8-10 | 371.0 | 0.16 | 1.81 | 0.16 | 24.75 | 0.809 |
| F1-8-11 | 448.0 | 0.19 | 2.22 | 0.19 | 28.31 | 0.639 |
| F1-8-22 | 555.3 | 0.26 | 1.60 | 0.25 | 26.84 | 0.700 |
| F1-8-32 | 718.0 | 0.31 | 0.58 | 0.30 | 24.79 | 0.807 |
| F1-8-50 | 912.8 | 0.39 | 5.23 | 0.38 | 22.54 | 0.969 |
| F1-8-52 | 964.5 | 0.46 | 5.58 | 0.41 | 21.03 | 1.122 |
| F1-8-61 | 985.3 | 0.45 | 7.36 | 0.39 | 21.7 | 1.049 |
| F1-8-77 | 762.0 | 0.35 | 5.08 | 0.29 | 20.15 | 1.234 |
| F1N-12 | 369.8 | 0.17 | 3.90 | 0.16 | 22.08 | 1.011 |
| F1N-25 | 577.2 | 0.27 | 2.72 | 0.25 | 24.25 | 0.840 |
| F1N-36 | 790.6 | 0.35 | 6.01 | 0.34 | 22.93 | 0.937 |
| F1N-40 | 829.9 | 0.36 | 1.85 | 0.33 | 22.57 | 0.967 |
| F1N-51 | 1284.4 | 0.59 | 1.26 | 0.47 | 20.57 | 1.178 |
| F1N-61 | 1284.4 | 0.60 | 1.26 | 0.41 | 20.37 | 1.204 |
| F1N-85 | 1269.5 | 0.60 | 11.46 | 0.45 | 19.44 | 1.343 |
| F2-12 | 310.7 | 0.14 | 4.45 | 0.14 | 18.57 | 1.508 |
| F2-26 | 433.0 | 0.19 | 10.83 | 0.19 | 24.05 | 0.854 |
| F2-30 | 540.8 | 0.24 | 5.40 | 0.23 | 23.91 | 0.863 |
| F2-41 | 719.8 | 0.32 | 3.58 | 0.30 | 23.44 | 0.897 |
| F2-48 | 1013.5 | 0.45 | 0.67 | 0.39 | 20.69 | 1.163 |
| F2-66 | 976.2 | 0.44 | 2.84 | 0.37 | 21.83 | 1.036 |
| F2-74 | 1396.7 | 0.62 | 15.35 | 0.50 | 19.95 | 1.262 |
| F2-94 | 1535.2 | 0.73 | 9.54 | 0.53 | 17.67 | 1.723 |

[a] $S_{BET}$ = BET surface area; $V_s$ and $S_{ext}$ = total pore volume and external surface area from $\alpha_s$ plot; $V_o$, $E_o$ and $L_o$ = micropore volume, characteristic energy and mean micropore width from DR plot.

found that $L_c$ decreases with increasing activation temperature of viscose rayon ACF [37], although Blanco-López et al. found no change for Nomex ACF [26]. Kaneko et al. reported a considerable increase from 0.8 to 4 nm on heating pitch or cellulose ACFs from 1473 K to 3173 K, although comparatively very little change was observed over the restricted range of temperatures below ~2000 K [30]. Morawski et al. found that doping of PAN with Fe(II) or Fe(III) provoked a considerable increase in the values of $L_c$ of the derived ACF from 1.4 nm up to 4–9 nm [41]. The titanium dioxide present in F2 evidently does not have the same sort of effect on the crystallite structure.

With regard to $L_a$, fewer results are available in the literature due to the diffuseness of the (*10*) peak, which makes accurate determination of the peak width difficult. With Kevlar ACF, $L_a$ appears to increase with burn-off [25], whereas with Nomex ACF Blanco-López et al. observed differences but were unable to define a tendency [26]. In contrast, our results show a clear increase. The absolute values are somewhat lower than those reported for Kevlar ACF [25], but much higher than those reported for pitch ACF [30–33]. Ishii et al. and Kaneko et al. have reported values for cellulose based ACF which are lower than ours [30,31], while Suzuki and Kaneko have reported higher values than ours [35]. Reported values for Nomex ACF are intermediate between our values for F1 and F1N, on the one hand, and F2, on the other [26].

In summary, the XRD results indicate that our acrylic

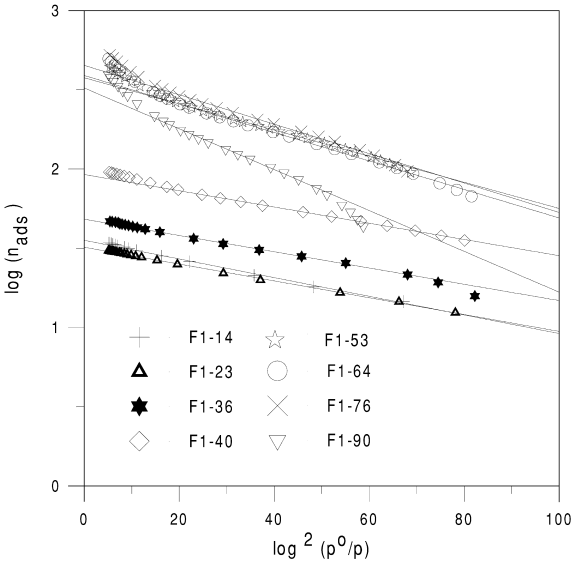


Fig. 10. Representative DR plots for F1.

ACF contain small plate-like turbostratic crystallites of size similar to that found with other PAN and Nomex ACFs. They are smaller than the crystallites found in Kevlar ACF, particularly with regard to their height, but larger than the crystallites found in pitch ACF, particularly with regard to their width.

### 5.2. Activation mechanism

Published values for rates of activation in $CO_2$ of ACFs include 0.5 mg $min^{-1}$ for Nomex ACF activated at 800°C [26], 0.7–1.2 mg $min^{-1}$ for Nomex activated at 850°C [26,27] and 1.8–2.4 mg $min^{-1}$ for Kevlar activated at 850°C [27]. Higher values, mainly in the range 5–15 mg $min^{-1}$, but with some values as high as 45 mg $min^{-1}$, have been obtained with viscose rayon cloths impregnated with boron oxo compounds or phosphates, and activated at 850°C [5,7]. It is not possible to make a direct quantitative comparison between these results and ours as the values obtained depend on the experimental conditions, such as flow-rate, temperature and mass of sample, used, as well as on the design of the furnace, and these parameters have been different in each case. For example, Blanco-López et al. used about half the mass of sample that we used and a flow rate about one half of ours, whereas Tomlinson et al. used flow rates about 50 times higher than we did [27] but sample masses which we believe to be about 6 times lower [56]. If all the results are expressed on a per gram basis, then our measured activation rates appear to be comparable to, although somewhat higher than, the previous work. The observation that our rates are somewhat higher could easily be explained on the basis of the higher temperature we used.

It would seem reasonable to conclude that the mechanism of activation of our samples is also similar to the mechanism of activation of other carbon materials. In general terms, this is believed to involve the burning out of amorphous carbon at low burn-offs, releasing porosity developed during carbonisation, followed by gasification at the edges, or other defect sites, of the pseudographitic sheets and eventual rearrangements of these sheets. We suggest that in the case of ACFs, over the first regime of activation in the present case, the less well organised (but not necessarily amorphous) carbon is being removed and that this eventually allows rearrangement, not only of individual pseudographitic sheets, but also of whole crystallites [30]. At low burn-off these rearrangements must be inhibited by bonds between crystallites involving heteroatoms or interlinked sheets. In the case of our sample F1, it is only at 40% burn-off that the structural rearrangements become possible and a number of parameters suddenly change at this point, including reactivity, stack height, pore volume and pore size. With F1N and F2, similar changes are observed, although they are less marked which suggests that in these cases some structural transformations begin to take place before 40% burn-off. This difference in behaviour could be indirectly associated with the higher AN content of F1 in comparison with F1N and F2.

At higher levels of burn-off, the amorphous carbon and most of the more reactive sites will have been removed and further activation must therefore involve attack on individual crystallites. The very low activation rates observed in the second regime may therefore be an indication that the crystallites of our samples are intrinsically more stable than those of Nomex or Kevlar ACF. It is also interesting to note that over a certain range of burn-offs all three samples have exactly the same activation rates which, bearing in mind the dimensional similarity of the crystallites in the three fibres, is consistent with the model proposed.

### 5.3. Porosity development

For the sample activated at 800°C the pore volume increases with burn-off, and reaches a maximum value of ~0.46 $cm^3$ $g^{-1}$ at slightly over 50% burn-off, before decreasing at higher levels of burn-off. The maximum pore volume is about 25% less than that achieved by activating at 900°C, although the mean pore width is not very different.

Much more interesting results were obtained with the samples activated at 900°C. Although the values of pore volume and pore width for these samples appear to be similar when the same burn-off is compared, there are also some rather interesting differences between them. Furthermore, the results indicate that the development of the porosity with increasing burn-off is not constant. These features can be seen most clearly from Figs. 11–13 where

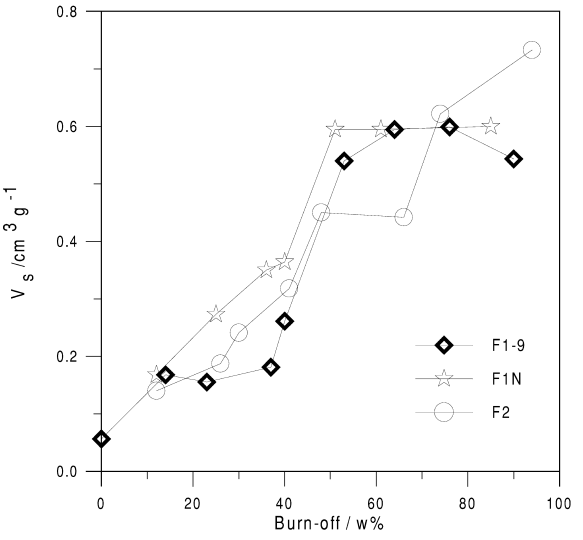


Fig. 11. Variation of $V_s$ with burn-off.

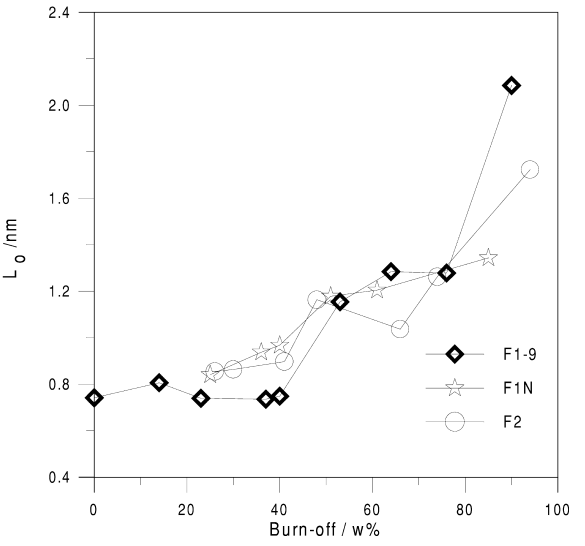


Fig. 13. Variation of $L_o$ with burn-off.

the pore volumes, $V_s$ and $V_o$, and the pore width, $L_o$, are represented graphically as a function of burn-off for the samples prepared by activation at 900°C.

Considering first fibre F1, it can be seen from Fig. 11 that the pore volume is approximately constant at ~0.17 $cm^3\ g^{-1}$ up to 40% burn-off, and then suddenly increases by a factor of 3 between 40 and 53%, and shows only a small variation thereafter. These results, which are quite unusual, suggest that most of the pore volume is blocked at low burn-offs. At around 40% burn-off the porosity rapidly becomes accessible, due to the removal of constrictions or, more likely, in view of the XRD results, rearrangements of the pseudographitic crystallites.

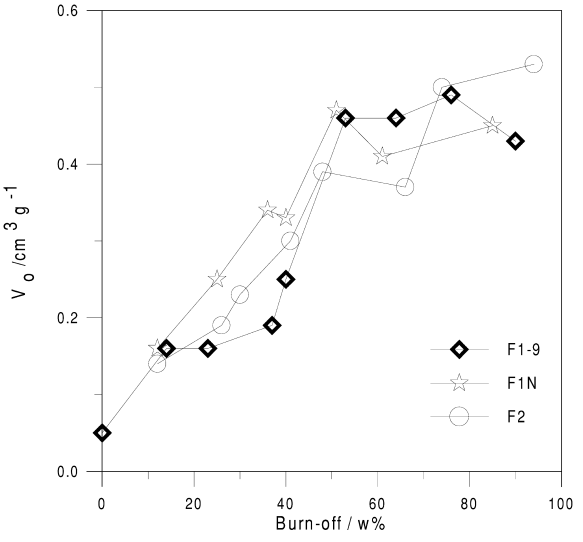


Fig. 12. Variation of $V_o$ with burn-off.

Similar behaviour is found with F1N and F2. At 10% burn-off they have the same pore volume as F1. However, from 10 to 40% burn-off, their pore volumes do not remain constant but increase. On the other hand, there is also a sudden increase in pore volume above 40% burn-off, although it is not as pronounced, as the porosity is not so effectively blocked at lower burn-offs. At high burn-off all three fibres give similar pore volumes, of the order of ~0.60 $cm^3\ g^{-1}$, the most significant difference being that the pore volume of F2 shows an additional increase at the highest burn-off studied.

The variation in $V_o$ as a function of burn-off, shown in Fig. 12, shows similar features to the variation in $V_s$, the most noteworthy difference being that the almost constant pore volume at higher burn-offs has the lower value of ~0.46 $cm^3\ g^{-1}$, indicating the presence of some wider micropores at the higher burn-offs.

From Fig. 13 it can be seen that the mean pore width also shows similar tendencies, although the behaviour is somewhat more complex. For F1 the mean pore width is ~0.75 nm and virtually constant up to 40% burn-off. It suddenly increases up to 1.15 nm at 53% burn-off, remains fairly constant up to 76% burn-off and then increases significantly up to 2.09 nm at 90% burn-off. With F1N and F2 the mean pore widths are slightly higher below 40% burn-off, but almost identical between ~50 and 80% burn-off, that is, over the second regime of activation it is not only the rate of activation which is equal for all three fibres, but also the pore widths, as well as the pore volumes $V_s$ and $V_o$.

Another interesting feature of Fig. 13 is the fact that the mean pore widths are apparently much higher for F2-12 and F1N-12. In the former case, as already mentioned, the isotherm was not completely in equilibrium at low

pressures. The concomitant reduction in amount adsorbed becomes increasingly less significant as the pressure increases. Hence, the isotherm becomes distorted, but the DR plot may still appear to be linear, in the sense of reduced amount adsorbed at low pressures. This will increase the slope of the DR plot leading to an overestimation of the mean pore width. The values indicated for F2-12 and F1N-12 are therefore not real values.

Another feature of the adsorption results is the fact that the range of linearity of the DR plots, such as the representative examples in Fig. 10, is limited at both low and high pressures when the burn-off is 53% or higher. As previously discussed in relation to the structural transformations occurring during the activation of viscose rayon cloths, this indicates that as well as the normal pore widening which occurs at higher burn-offs, there is also a narrowing of some of the pores [39]. This pore narrowing is associated with the structural rearrangements of the crystallites and also with the shrinkage of the fibre which occurs during the thermal treatments.

Finally, we can compare our results with others in the literature. The micropore volumes obtained are much higher than those obtained with Kevlar and, at the 50–60% burn-off level, higher than those obtained with Nomex. At low burn-off, our mean pore sizes are ~0.1 nm lower than those found with Nomex. On the other hand, at high burn-off our mean pore sizes are ~0.1 nm higher. None of these fibres currently compares favourably with viscose rayon ACF which can have much higher pore volume, greater than 1 $cm^3 g^{-1}$, and whose pore size can be controlled within the range 0.5 nm up to the small mesopore range, depending on the conditions of preparation. Very high pore volumes are also possible with pitch ACF but only at the expense of greater pore width.

## 6. Conclusions

The results presented show that acrylic textile fibres can be used to produce ACF with properties which compare favourably with those of non-textile PAN, Kevlar and Nomex ACF. As would be expected, it was found that the exact microstructural characteristics of the ACF depend on the precise nature of the precursor and the conditions of carbonisation and activation. In addition, the results obtained seem to indicate that the fibre processing may also influence the development of the structure during activation. Another important aspect is the role of 'amorphous carbon' and heteroatoms. It is well known that amorphous carbon blocks the incipient microporosity developed during carbonisation. Our results, in particular with fibre F1 activated at 900°C, indicate that at least some of the carbon and other atoms which are not included in the initially formed microcrystallites inhibit their movements, presumably because they form rigid crosslinks between the microcrystallites. These atoms are more reactive than the atoms within the microcrystallites and as they are progressively burnt out during activation reorganisation of the microcrystallites becomes possible.

## Acknowledgements

The authors are grateful to Diego Álvarez, Amélia Martínez Alonso, Fabian Garcia and Juán Tascón for their invaluable assistance during the time JMVN spent at INCAR, where the XRD and SEM measurements were carried out, to FISIPE-Fibras Sintéticas de Portugal for the provision of samples and to the Fundação para a Ciência e a Tecnologia (Portugal), the Fundo Europeu para o Desenvolvimento Regional (FEDER) and program PRAXIS XXI (project no. PRAXIS/3/3.1/MMA/1781/95) for financial support.

## References

[1] Mays T. Active carbon fibers. In: Burchell TD, editor, Carbon materials for advanced technologies, Oxford: Pergamon Press, 1999, pp. 95–118.
[2] Suzuki M. Activated carbon fiber: fundamentals and applications. Carbon 1994;32(4):577–86.
[3] Mochida I, Korai Y, Shirahama M, Kawano S, Hada T, Seo Y, Yoshikawa M, Yasutake A. Removal of $SO_x$ and $NO_x$ over activated carbon fibers. Carbon 2000;38(2):227–39.
[4] Freeman JJ, Gimblett FGR, Roberts RA, Sing KSW. Studies of activated charcoal cloth. I. Modification of adsorptive properties by impregnation with boron-containing compounds. Carbon 1987;25(4):559–63.
[5] Freeman JJ, Gimblett FGR. Studies of activated charcoal cloth. II. Influence of boron-containing impregnants on the rate of activation in carbon dioxide gas. Carbon 1987;25(4):565–8.
[6] Freeman JJ, Gimblett FGR, Roberts RA, Sing KSW. Studies of activated charcoal cloth. III. Mesopore development induced by phosphate impregnants. Carbon 1988;26(1):7–11.
[7] Freeman JJ, Gimblett FGR. Studies of activated charcoal cloth. IV. Influence of phosphate impregnants on the rate of activation in carbon dioxide gas. Carbon 1988;26(4):501–5.
[8] Freeman JJ, Gimblett FGR, Sing KSW. Studies of activated charcoal cloth. V. Modification of pore structure by impregnation with certain transition metal salts and oxo-complexes. Carbon 1988;26(1):7–11.
[9] Zhang YZ, Wang MZ, He F, Zhang BJ. Mesopore development in PAN–ACF resulting from non-metal additives. J Mat Sci 1997;32:6009–13.
[10] Koresh JE, Soffer A. Molecular sieve carbon permselective membrane. Part I. presentation of a new device for gas mixture separation. Separ Sci Technol 1983;18(8):723–34.
[11] Jones CW, Koros WJ. Carbon molecular sieve gas separation membranes — I. Preparation and characterization based on polyimide precursors. Carbon 1994;32(8):1419–25.
[12] Burchell TD. Porous carbon fiber-carbon binder composites.

In: Burchell TD, editor, Carbon materials for advanced technologies, Oxford: Pergamon Press, 1999, pp. 169–203.
[13] Lee JC, Lee BH, Kim BG, Park MJ, Lee DY, Kuk IH, Chung H, Kang HS, Lee HS, Ahn DH. The effect of carbonization temperature of PAN fiber on the properties of activated carbon fiber composites. Carbon 1997;35(10–11):1479–84.
[14] Wan Y, Wang Y, Wen T. Effect of specific surface area and silver content on bacterial adsorption onto ACF(Ag). Carbon 1999;37:351–8.
[15] Li C, Wan Y, Wang J, Wang Y, Jiang X, Han L. Antibacterial pitch-based activated carbon fiber supporting silver. Carbon 1998;36(1–2):61–5.
[16] Oya A, Yoshida S, Alcañiz-Monge J, Linares-Solano A. Preparation and properties of an antibacterial activated carbon fiber containing mesopores. Carbon 1996;34(1):53–7.
[17] Alcañiz-Monge J, Casa-Lillo M, Cazorla-Amorós D, Linares-Solano A. Methane storage in activated carbon fibres. Carbon 1997;35(2):291–7.
[18] Yoshida A, Tanahashi I, Nishino A. Effect of concentration of surface acidic functional groups on electric double-layer properties of activated carbon fibers. Carbon 1990;28(5):611–5.
[19] Ling L, Li K, Liu L, Miyamoto S, Korai Y, Kawano S, Mochida I. Removal of $SO_2$ over ethylene tar pitch and cellulose based activated carbon fibers. Carbon 1999;37:499–504.
[20] Daley M, Mangun C, deBarr J, Riha S, Lizzio A, Donnals G, Economy J. Adsorption of $SO_2$ onto oxidized and heat-treated activated carbon fibers (ACFS). Carbon 1997;35(3):411–7.
[21] Stoeckli F, Centeno TA, Fuertes AB, Muñiz J. Porous structure of polyarylamide-based activated carbon fibres. Carbon 1996;34(10):1201–6.
[22] Mangun C, Daley M, Braatz R, Economy J. Effect of pore size on adsorption of hydrocarbons in phenolic-based activated carbon fibers. Carbon 1998;36(1–2):123–31.
[23] Daley MA, Tandon D, Economy J, Hippo EJ. Elucidating the porous structure of activated carbon fibers using direct and indirect methods. Carbon 1996;34(10):1191–200.
[24] Dresselhaus MS, Fung AWP, Rao AM, di Vittorio SL, Kuriyama K, Dresselhaus G, Endo M. New characterization techniques for activated carbon fibers. Carbon 1992;30(7):1065–73.
[25] Cuesta A, Martínez-Alonso A, Tascón JMD, Bradley RH. Chemical transformations resulting from pyrolysis and $CO_2$ activation of Kevlar flocks. Carbon 1997;35(7):967–76.
[26] Blanco López MC, Martínez-Alonso A, Tascón JMD. Microporous texture of activated carbon fibres prepared from Nomex aramid fibres. Mic Mes Mat 2000;34:171–9.
[27] Tomlinson JB, Freeman JJ, Sing KSW, Theocharis CR. Rates of activation and scanning electron microscopy of polyarylamide-derived chars. Carbon 1995;33(6):789–93.
[28] Freeman JJ, Tomlinson JB, Sing KSW, Theocharis CR. Adsorption of nitrogen and water vapour by activated Nomex chars. Carbon 1995;33(6):795–9.
[29] Martínez-Alonso A, Jamond M, Montes-Morán M, Tascón JMD. Microporous texture of activated carbon fibers prepared from aramid fiber pulp. Micropor Mat 1997;11(5–6):303–11.
[30] Kaneko K, Ishii C, Ruike M, Kuwabara H. Origin of superhigh surface area and microcrystalline graphitic structures of activated carbons. Carbon 1992;30(7):1075–88.
[31] Ishii C, Suzuki T, Shindo N, Kaneko K. Structural characterization of heat-treated activated carbon fibers. J Por Mat 1997;4:181–6.
[32] Sato M, Sukegawa T, Suzuki T, Kaneko K. Surface fractal dimension of less-crystalline carbon micropore walls. J Phys Chem B 1997;101:1845–50.
[33] el Merraoui M, Tamai H, Yasuda H, Kanata T, Mondori J, Nadai K, Kaneko K. Pore structures of activated carbon fibers from organometallics/pitch composites by nitrogen adsorption. Carbon 1998;36(12):1769–76.
[34] Gondy D, Ehrburger P. Swelling of pitch-based carbon fibres during activation in carbon dioxide. Carbon 1997;35(12):1745–51.
[35] Suzuki T, Kaneko K. The micrographite growth of activated carbon fibers with high temperature treatment studied by computer-aided X-ray diffraction. Carbon 1993;31(8):1360–1.
[36] Wang Y, Wan Y, Dong X, Cheng G, Tao H, Wen T. Preparation and characterization of antibacterial viscose-based activated carbon fiber supporting silver. Carbon 1998;36(11):1567–71.
[37] Kumar K, Saxena RK, Kothari R, Suri DK, Kaushik NK, Bohra JN. Correlation between adsorption and X-ray diffraction studies on viscose rayon based activated carbon cloth. Carbon 1997;35(12):1842–4.
[38] Brasquet C, Lecloirec P. Adsorption onto activated carbon fibers: application to water and air treatments. Carbon 1997;35(9):1307–13.
[39] Carrott PJM, Freeman JJ. Evolution of micropore structure of activated charcoal cloth. Carbon 1991;29(4/5):499–506.
[40] Mori M, Aori K, Isoda T, Omotehara Y, Anpo M. Removal of diluted NO using activated carbon fibers. Nippon Kagaku Kaishi 1997;2:147–52.
[41] Morawski AW, Kalucki K, Nakashima M, Inagaki M. Modified carbonization of polyacrylonitrile by incorporation of $FeCl_2$ and $Fe(NO_3)_3$-pore structure. Carbon 1994;32(8):1457–61.
[42] Ryu Z, Zheng J, Wang M. Porous structure of PAN-based activated carbon fibers. Carbon 1998;36(4):427–32.
[43] Ryu Z, Zheng J, Wang M, Zhang B. Characterization of pore size distributions on carbonaceous adsorbents by DFT. Carbon 1999;37:1257–64.
[44] Kakida H, Tashiro K, Kobayashi M. Mechanism and kinetics of stabilization reactions of polyacrylonitrile and related copolymers I. Relationship between isothermal DSC thermogram and FTIR spectral change of an acrylonitrile/methacrylic acid copolymer. Polymer J 1996;28(1):30–4.
[45] Kakida H, Tashiro K. Mechanism and kinetics of stabilization reactions of polyacrylonitrile and related copolymers III. Comparison among the various types of copolymers as viewed from isothermal DSC thermograms and FTIR spectral changes. Polymer J 1997;29(7):557–62.
[46] Coleman MM, Sivy GT. Fourier transform IR studies of the degradation of polyacrylonitrile copolymers — I. Introduction and comparative rates of the degradation of three copolymers below 200°C and under reduced pressure. Carbon 1981;19:123–6.
[47] Sivy GT, Coleman MM. Fourier transform IR studies of the degradation of polyacrylonitrile copolymers — II. Acrylonitrile/methacrylic acid copolymers. Carbon 1981;19:127–31.
[48] Coleman MM, Sivy GT. Fourier transform IR studies of the degradation of polyacrylonitrile copolymers — III.

Acrylonitrile/vinyl acetate copolymers. Carbon 1981;19:133–5.
[49] Sivy GT, Coleman MM. Fourier transform IR studies of the degradation of polyacrylonitrile copolymers — IV. Acrylonitrile/acrylamide copolymers. Carbon 1981;19:137–9.
[50] Watt W. Carbon work at the Royal Aircraft Establishment. Carbon 1972;10:121–43.
[51] Donnet J-B, Wang TK, Rebouillat S, Peng JCM, editors, Carbon fibers, 3rd ed, New York: Marcel Dekker, 1998.
[52] Táscon JMD. Estruturas y formas del carbono en estado sólido. In: Short Course: Introducción a la quimica y tecnologia de materiales de carbono, Oviedo (Spain): INCAR, 1999.
[53] Oberlin A, Bonnamy S, Lafdi K. Structure and texture of carbon fibers. In: Donnet J-B, Wang TK, Rebouillat S, Peng JCM, editors, Carbon Fibers, 3rd ed, New York: Marcel Dekker, 1998, chapter 2.
[54] Carrott PJM, Roberts RA, Sing KSW. Standard nitrogen adsorption data for nonporous carbons. Carbon 1987;25(6):769–70.
[55] Stoeckli HF, Rebstein P, Ballerini L. On the assessment of microporosity in active carbons, a comparison of theoretical and experimental data. Carbon 1990;28(6):907–9.
[56] Freeman JJ. Studies in the development and modification of the pore structure in activated viscose rayon chars, Brunel University, 1986, PhD Thesis.